ACS OMEGA

http://pubs.acs.org/journal/acsodf

Article

# Phase-Selective and Localized $TiO_2$ Coating on Additive and Wrought Titanium by a Direct Laser Surface Modification Approach

Parvin Fathi-Hafshejani, Haden Johnson, Zabihollah Ahmadi, Michael Roach, Nima Shamsaei, and Masoud Mahjouri-Samani*

Cite This: *ACS Omega* 2020, 5, 16744−16751

Read Online

ACCESS | Metrics & More | Article Recommendations | Supporting Information

**ABSTRACT:** Titanium has been the material of interest in biological implant applications due to its unique mechanical properties and biocompatibility. Their design is now growing rapidly due to the advent of additive manufacturing technology that enables the fabrication of complex and patient-customized parts. Titanium dioxides ($TiO_2$) coatings with different phases (e.g., anatase, rutile) and morphologies have shown to be effective in enhancing osteointegration and antibacterial behavior. This enhanced antibacterial behavior stems from the photocatalytic activity generated from crystalline $TiO_2$ coatings. Anatase has commonly been shown to be a more photocatalytic oxide phase compared to rutile despite its larger band gap. However, more recent studies have suggested that a synergistic effect leading to increased photocatalytic activity may be produced with a combination of oxides containing both anatase and rutile phases. Here, we demonstrate the selective and localized formation of $TiO_2$ nanostructures on additive and wrought titanium parts with anatase, rutile, and mixed phases by a laser-induced transformation approach. Compared to conventional coating processes, this technique produces desired $TiO_2$ phases simply by controlled laser irradiation of titanium parts in an oxygen environment, where needed. The effects of processing conditions such as laser power, scanning speed, laser pulse duration, frequency, and gas flow on the selective transformation were studied. The morphological and structural evolutions were investigated using various characterization techniques. This method is specifically of significant interest in creating phase-selective $TiO_2$ surfaces on titanium-based bioimplants, including those fabricated by additive manufacturing technologies.

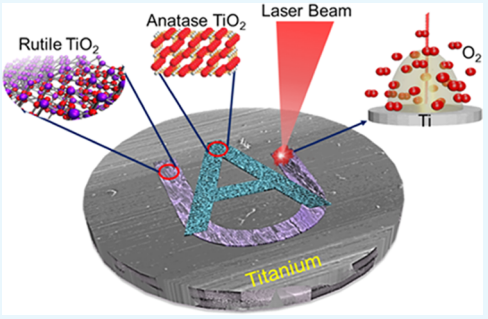


## INTRODUCTION

Titanium-based parts and implants are widely used in the field of orthopedic and dental surgery because of their appropriate biocompatibility and mechanical properties such as bio-inertness, low allergenicity, excellent fatigue life, and good strength-to-weight ratio.[1−3] The design of such implants is growing rapidly with the advent of additive manufacturing technology that enables the fabrication of complex and patient-customized parts.[4] Many recent efforts have been made to modify and functionalize the surface of titanium-based implants.[5−13] Improving the antibacterial activity of titanium dioxide ($TiO_2$) coatings on implant materials has been reported as an attractive natural solution for improving implant surfaces,[14−16] for example, by depositing $TiO_2$ nanoparticles or nanotubes on the surface of titanium parts.[17]

$TiO_2$ nanomaterials are widely used in applications ranging from photocatalysis and energy to biomedical and sensing devices.[18] Their physical properties are strongly correlated to their phases (e.g., anatase, rutile, brookite, amorphous),[19] and morphologies (e.g., micro/nanostructures, porosity).[20−22] Thus, various surface oxidation methods, such as chemical (acid and alkali) treatment, sol−gel formation, ion implantation, and thermal oxidation, have been employed to develop a functional implant surface by changing the surface properties of the native passive layer to improve osseointegration.[23−28] Various physical, chemical, or electrochemical deposition processes are used for the synthesis of $TiO_2$ structures and films on titanium parts such as electrochemical anodization, chemical vapor deposition, pulse laser deposition, thermal and plasma spray, and sputtering techniques.[19,29−37]

Anodization is a technique that expands the thickness of the natural oxide layer on the surface of metal components.[38] These methods have been successful in providing uniform coatings of specific $TiO_2$ phases.[39−41] Anodized anatase surfaces have commonly shown higher photocatalytic activity than rutile surfaces leading to an enhanced antimicrobial effect.[42−44] More recent studies have shown mixed-phase oxides, containing both anatase and rutile, to exhibit a synergistic effect with increased photocatalytic activity.[45,46] In

Received: April 12, 2020
Accepted: June 18, 2020
Published: July 2, 2020









https://dx.doi.org/10.1021/acsomega.0c01671
*ACS Omega* 2020, 5, 16744−16751

mixed-phase oxides, differences in the band gaps extend the lifetime of the electron−hole pairs and thus increase the generation of free radicals.[47] For this synergistic effect to occur, the anatase and rutile phases need to be in close spatial proximity to each other. Anodization methods are not able to provide localized, phase-selective, and patterned coatings, especially on parts with complex geometries. Therefore, the development of a facile method that allows the formation of phase-specific, location-specific, and patternable $TiO_2$ nanostructures on the complex titanium parts is highly desirable for the medical sector.

Additionally, the complexity of the implants' shape and multi-interfaces with various tissues in the body requires the ability to selectively and locally deposit specific phases and morphologies of $TiO_2$ on various locations of implants, making it extremely challenging using conventional coating methods. This is specifically true for additively manufactured implants that can be customized per patient and injury. The freedom in design offered by additive manufacturing technologies is revolutionizing the implant industry by introducing customized implants that often have more complex geometries. Due to such complexities, not only are more location-specific depositions needed, but it also requires an accurate method to precisely deposit on confined regions of the implant.

Here, we report a novel laser processing method for localized, phase-selective, and pattered $TiO_2$ nanostructures directly on the titanium samples as desired. In this method, a tunable nanosecond fiber laser (1064 nm wavelength) with pulse widths ranging from 5 to 2000 ns, pulse energy ranging from 0.04 to 1.57 mJ, and a repetition rate ranging from 1 Hz to 4160 kHz was used for the controlled surface modifications. The laser beam was coupled into a galvo scanner with an F-theta lens providing an 18 $\mu$m focal size and a scan speed ranging from 1 to 5000 mm/s. This allowed us to locally process the titanium parts in a controlled oxygen environment to accurately induce structural, chemical, and phase transformations. After reactions, a thin film of $TiO_2$ nanoparticles formed on the titanium parts. By tuning the processing parameters, different $TiO_2$ phases (e.g., rutile, anatase, mixed) and patterns were generated on the surfaces of titanium samples where desired.

## RESULTS AND DISCUSSION

Lasers provide the ability to accurately deliver a precise amount of energy onto a confined region of a material to achieve the desired response. For opaque materials, this energy is absorbed near the surface, modifying the surface chemistry, crystal structure, and/or multiscale morphology without altering the bulk material. The nonequilibrium processes in the high-energy laser-material interaction dynamics can overcome energy barriers required for chemical reactions and increase their reaction kinetics far beyond equilibrium processes.[48−50] In this method, irradiation of the material with a short laser leads to rapid heating of the surface of the material and the formation of high-temperature plasma that prepares the bed for oxygen dissociation and its reaction with titanium. With this dry and clean technique, high-purity $TiO_2$ coatings with controlled phases and morphologies can be synthesized on the surface of titanium samples. Figure 1 shows the schematic illustration of the fabrication process. By scanning the titanium surface with this tunable laser, titanium and oxygen controllably react to form the porous structures of $TiO_2$ with specific phases on the surface of the titanium

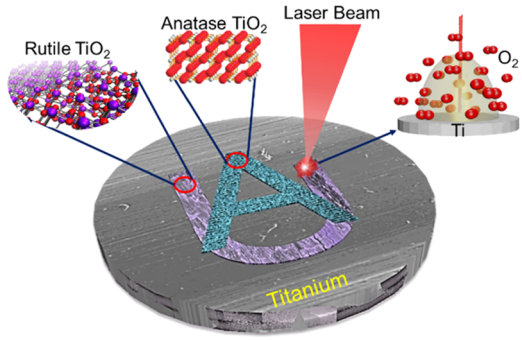


**Figure 1.** Schematic illustration showing the patterned, localized, and phase-selective fabrication of anatase and rutile $TiO_2$ nanostructures on the titanium samples by a controlled laser surface modification approach.

sample. A comprehensive experimental study was performed to understand and control this process.

We first focused on understanding how the laser parameters, and, hence, the surface-coupled energy can govern the evolution of the phase and morphology of the formed $TiO_2$ micro/nanostructures. The amount of coupled energy in this process is mainly the combination of pulse width, focus point, repetition rate, and scan speed of the laser. Therefore, we performed a systematic study under various process parameters including laser power ranging from 13 to 71 W with six scan speeds (100, 200, 500, 1000, 2000, 5000 mm/s), and six factory-set pulse widths (10, 108, 261, 508, 1020, 2020 ns). Through these studies, we demonstrated the crystallization dynamics, identified the energy thresholds, and found all possible transformation and noninteracting zones. Four types of titanium samples, including additive manufactured and commercial wrought TAV (Ti−6Al−4V Grade 5), CP titanium Grade 4, and pure titanium (99.99% purity), were tested in this study.

Figure 2 shows the effect of laser power, scan speed, and pulse width on the formation of anatase, rutile, and mixed-phase on the titanium samples. Figure 2a shows a heatmap of the unaffected, anatase, mixed anatase/rutile, and rutile formation zones as a function of laser power and scan speed using a laser pulse width of 508 nm and a PRF0 frequency of 108 kHz on pure titanium sheets (purity 99.99%). The line hatch has 40% overlap, while the pulse overlap (pitch) varies by the scan speed. In this case, the energy per pulse ranges from 0.125 mJ for 13.5 W power to 0.687 mJ for 74 W power with the fluence of 47 and 270 J/cm$^2$, respectively. It should be noted that the energy per pulse is constant for all of the frequencies used in this work since the chosen frequencies are below the PRF0 value for each waveform, according to the laser operating manual. PRF0 is the minimum frequency that gives maximum average power (defined by the active current setpoint). For PRF > PRF0, pulse energies and peak powers decrease so that the average power does not exceed the rated power of the laser module.

In general, higher laser powers and/or slower scan speeds tend to induce rutile formation by inducing more heat, while lower laser power and/or faster scan speed change the kinetics toward the anatase formation zone by inducing less heat. It was observed that the rutile zone (red), where the best quality rutile crystals form, was much wider than the anatase and mixed-phase zones. Above this red zone, due to extreme temperatures, samples ignite and burn. As it is apparent from


https://dx.doi.org/10.1021/acsomega.0c01671
ACS Omega 2020, 5, 16744−16751

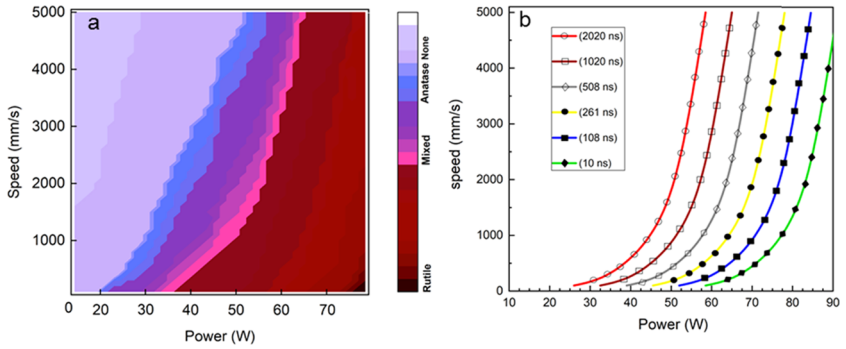


**Figure 2.** Comprehensive map (a) of the pure titanium (purity 99.99%) response to different laser powers and scan speeds under atmospheric oxygen pressure and 0.1 SLM oxygen flow. Blue, red, and purple zones show the process regions where anatase, rutile, and mixed phases form during the process, respectively. The effect of the pulse width on the transformation process (b). The lines in (b) indicate the anatase to rutile transition boundary, where mixed rutile and anatase phases coexist. Pure anatase and rutile phases exist to the left and right of the lines for each waveform, respectively.

**Table 1. Laser Parameters to Synthesize Different Titanium Phases**

| $TiO_2$ phase | laser power (W) | scan speed (mm/s) | pulse width (ns) | pulse energy (mJ) | pulse fluence ($J/cm^2$) | gas flow rate (SLM) | pulse overlap (%) | line hatch (%) | frequency (kHz) |
|---|---|---|---|---|---|---|---|---|---|
| anatase | 12.5 | 400 | 508 | 0.625 | 246 | 25.6 | 0 | 40 | 20 |
| mixed | 67.5 | 400 | 508 | 0.337 | 133 | 25.6 | 50 | 0 | 200 |
| rutile | 62.5 | 200 | 508 | 0.625 | 246 | 21.3 | 90 | 0 | 100 |

the narrow crystallization window of the anatase (blue), its formation required a very deliberate process parameter control that otherwise could easily transform into mixed or rutile phases. The process parameter zone in between anatase and rutile generated mixed anatase/rutile phases (purple). Furthermore, the pulse-width study (Figure 2b) showed that increasing the pulse duration would result in a left shift in the power and speed relationship plots. This infers that the longer pulse durations induce more heat than that of shorter pulses, which in turn requires less power or more speed to balance the required transformation energies in each zone.

We further studied the effect of distance between the processing lines (hatch) and overlap between the pulses (overlapping). We found that these processing parameters have a significant impact on the phase and morphology evolution of the final $TiO_2$ structures. In addition, the role of the laser repetition rate (frequency) that dictates the time between the consecutive pulses was found to be important in the transformation process. For instance, at lower frequencies (e.g., 20 kHz), the off-time between the pulses increases, providing more cooling time before the next pulse arrives. This fast heat quenching of the reaction in each pulse resulted in the formation of anatase nanoparticles that stick well to the surface. We, therefore, designed a systematic experiment to track the impact of overlapping pulses and the off-time between the consecutive pulses employing the best speed and power parameters found in the previous experiment, which could produce better anatase, rutile, and mixed phases.

As expected, at lower frequencies (e.g., 20 kHz), the off-time between pulses is 49.5 $\mu$s, which provides the material enough time to cool between the pulses resulting in the formation of high-quality anatase structures. At higher frequencies (e.g., 100 kHz), the off-time between pulses becomes 9.5 $\mu$s, resulting in heat accumulation, and, hence, the formation of high-quality rutile $TiO_2$ structures. It should be noted that the energy per pulse does not change by changing the repetition rate as long as it is below the maximum allowable frequency defined by the manufacturer (SPI Lasers). Similarly, using less overlap (e.g., 0%) between the processed spots formed anatase structures, while more overlap (e.g., 90%) formed rutile structures due to the overheating/reheating. In addition, reprocessing of the formed anatase phase transformed it into the rutile phase. Table 1 shows an example of the optimized process parameters by which the high-quality anatase, rutile, and mixed-phase $TiO_2$ coatings were produced, according to Raman and X-ray diffraction (XRD) measurements described below. Although Table 1 was optimized for wrought TAV samples, the same set of parameters were also tested on wrought CP Ti, additive, and pure titanium (see the Supporting Information) that created similar expected results. The results on the wrought CP Ti samples were comparable and had the same quality results as wrought TAV. The results on the additive and pure titanium samples could be further improved by fine-tuning these parameters.

To monitor the transformation process and identify the formed $TiO_2$ phases on the titanium samples, we performed Raman and glancing angle XRD spectroscopy. Also, to evaluate the quality of our laser-generated $TiO_2$ samples, their Raman signatures were compared with that of commercially available anatase and rutile powders, both showing similar signatures (see the Supporting Information). The Raman spectra were acquired using a 532 nm laser excitation source, a 10× objective lens, and 1200 lines/mm grating. Figure 3a shows the Raman spectra obtained from the anatase, rutile, and mixed-phase in this experiment. Anatase samples showed clear Raman peaks at 145, 198, 399, 516, and 638 $cm^{-1}$, while rutile samples showed peaks at 241, 445, 610 $cm^{-1}$. The samples with mixed phases have the signature of both anatase and rutile. These Raman results were similar to the results reported in the literature,[51] confirming the successful formation of various $TiO_2$ phases in this process. The transformation quality was similar for all samples used in this experiment, including additively manufactured and wrought TAV, wrought CP Ti Grade 4, and pure titanium samples.


https://dx.doi.org/10.1021/acsomega.0c01671
ACS Omega 2020, 5, 16744−16751

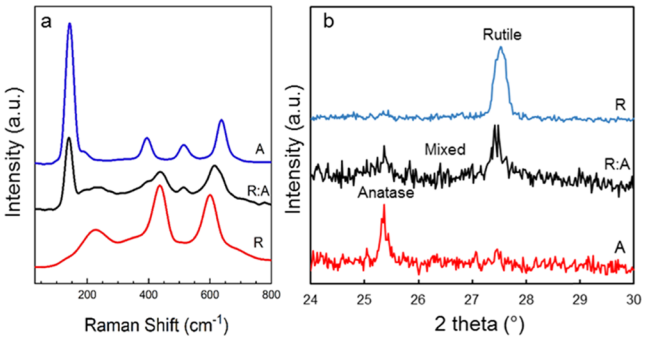


**Figure 3.** Representative Raman spectra (a) and XRD scans (b) of the synthesized $TiO_2$ structures on wrought TAV samples showing the successful formation of anatase, mixed-phase, and rutile peaks.

Figure 3b shows the XRD results from wrought TAV samples. Peaks at 25.3°, which verify the presence of anatase phase, are present on the anatase and mixed-phase specimens. The peak at 27.5° on rutile and mixed-phase specimens confirms the formation of rutile. The weight fractions of anatase and rutile in the oxide layer of representative specimens from each group were calculated using the following Spurr and Myers equation[52]

$$X_A = \frac{1}{1 + 1.26\left(\frac{I_R}{I_A}\right)}$$

$$X_R = 1 - X_A$$

where $X_R$ and $X_A$ are the weight percentages of rutile and anatase, and $I_R$ and $I_A$ are the intensities of the diffraction peaks for rutile (110) and anatase (101), respectively. The phase ratio for the mixed-phase oxide shown in Figure 3b was 37% anatase and 63% rutile. Similar results were also obtained for the additively manufactured and pure titanium samples (see the Supporting Information). These results verify and support the findings observed using Raman spectroscopy.

To analyze the surface morphology and physical structure of the synthesized $TiO_2$ samples in this process, we performed optical microscopy, laser confocal microscopy, and scanning electron microscopy (SEM) to obtain information at various length scales. Figure 4a–f shows the laser confocal two-dimensional (2D) images (a, c, e) and corresponding three-dimensional (3D) surface profiles (b, d, f) of the synthesized anatase, mixed-phase, and rutile samples, respectively. Representative surface roughness ($R_a$) values for anatase, mixed-phase, and rutile wrought TAV samples were 5.17, 4.69, and 4.72 $\mu$m, respectively. Optical microscopy images for additively manufactured TAV and pure titanium (purity 99.99%) samples have been shown in Figures S2 and S5 of the Supporting Information.

Figure 5 shows the SEM images of the anatase, mixed-phase, and rutile $TiO_2$ formed on the surface of wrought TAV samples. The size and morphology of the anatase samples were micro/nanostructures with a porous morphology, as shown in Figure 5a,b. As seen in Figure 5e,f, the rutile $TiO_2$ on wrought TAV were larger crystals with big cracks showing the ceramic nature of the rutile structures. Additionally, both cracks and porous structures were produced on the mixed-phase surface,

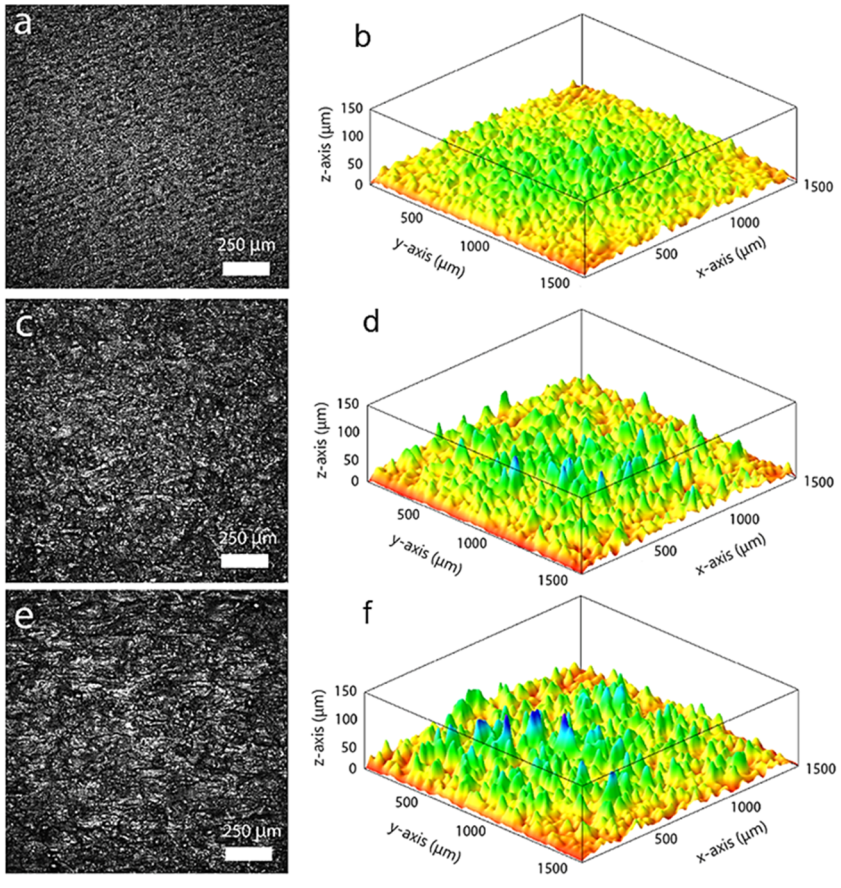


**Figure 4.** Laser confocal 2D images and 3D surface profiles of anatase (a, b), mixed-phase (c, d), and rutile (e, f) $TiO_2$ wrought TAV samples.



https://dx.doi.org/10.1021/acsomega.0c01671
ACS Omega 2020, 5, 16744−16751

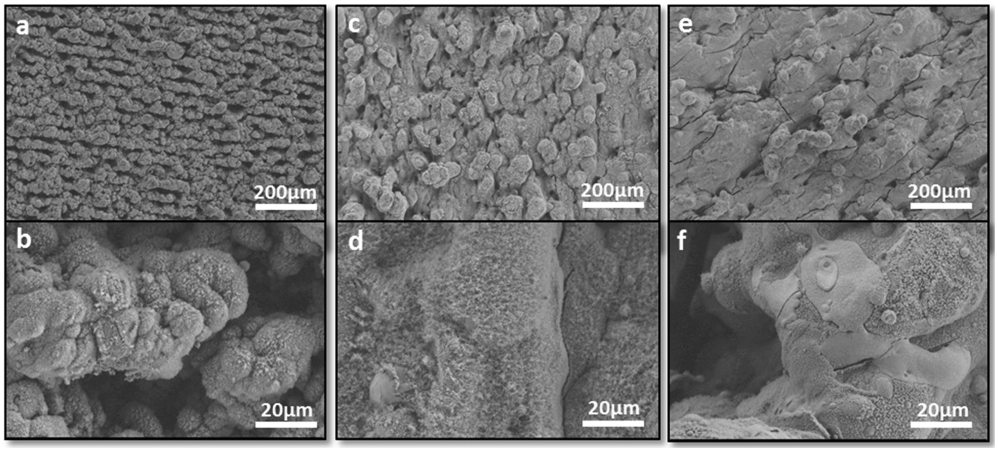


**Figure 5.** SEM images showing the morphology of the wrought TAV $TiO_2$ anatase (a, b), mixed-phase (c, d), and rutile (e, f) nanostructures. Smaller features with micro/nanostructures and a mesoporous morphology were observed for anatase samples. The feature became larger and denser for rutile samples.

as shown in Figure 5c,d. SEM images for titanium sheets (purity 99.99%) and additive manufactured samples show a similar trend (see the Supporting Information). Based on the cross-section SEM images of the laser-modified wrought TAV, the anatase layer looked mesoporous with a thickness of ~0.2−0.5 $\mu$m, whereas the thickness of the mixed-phase and rutile became gradually thicker with ~0.4 and ~2 $\mu$m, respectively (see the Supporting Information).

One of the most noticeable advantages of this method, specifically for the customized additive manufactured implants, is its ability for the selective and localized synthesis of various phases, shapes, sizes, and patterns side-by-side without the need for any conventional patterning or lithography and deposition processes. This unique laser processing method allows us to design desired $TiO_2$ structures on beneficial locations on the bioimplant surfaces. We have successfully synthesized rutile, anatase, and mixed-phase $TiO_2$ structures with designed patterns and matrices. Figure 6a−c shows the optical images of various rutile/anatase patterns side-by-side in checkerboard, concentric circles, and AU logo designs. Figure 6d,e shows the corresponding Raman spectra obtained from anatase and rutile as labeled.

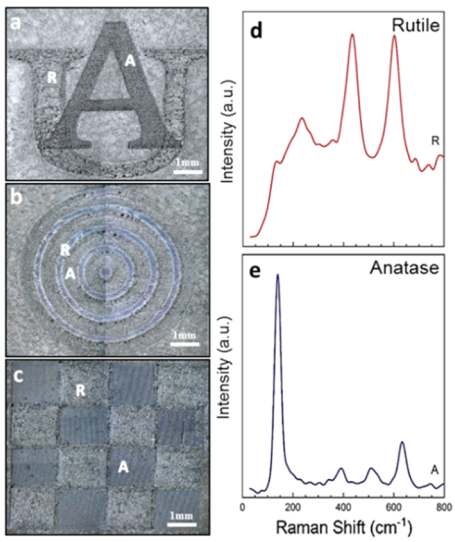


**Figure 6.** Selective and localized formation of anatase and rutile $TiO_2$, side-by-side. Optical images show Auburn University logo (a), concentric circular patterns (b), and checkerboard (c) consisting of anatase and rutile $TiO_2$, side-by-side. Representative Raman spectra obtained from the rutile (d) and anatase (e) regions as labeled.

## CONCLUSIONS

In conclusion, we demonstrated the localized, selective, and patterned synthesis of various $TiO_2$ phases and structures by controlled laser transformation of titanium surface. Anatase, mixed-phase, and rutile $TiO_2$ were formed by precisely tuning the laser interaction with titanium in an oxygen environment. The laser interaction with titanium was controlled by the laser power, scan speed, and pulse width. We showed that longer pulse widths, slower scan speeds, and higher laser powers led to the formation of rutile phases, while shorter pulse widths, lower laser powers, and faster scan speeds resulted in the formation of anatase $TiO_2$. Processing parameters in between formed mixed rutile/anatase $TiO_2$. We also showed the effect of the overlapping of pulses on the phase transformation. More overlaps resulted in the phase transformation toward rutile $TiO_2$ and vice versa. This method offers a simple, clean, and fast formation of $TiO_2$ coating on titanium bioimplants, specifically the customized, additively manufactured ones, with the preferred phases, structures, and patterns where desired.

## MATERIALS AND METHODS

**Sample Preparation.** We used four different types of titanium products, including pure titanium (purity 99.99%) sheets (10 × 10 mm squares, 1000 test surfaces), additively manufactured (10 mm in diameter, 60 test surfaces), wrought TAV (15 mm in diameter, 30 test surfaces), and CP Ti Grade 4 (15 mm in diameter, 30 test surfaces) samples in these experiments. CP Ti Grade 4, TAV, and pure titanium were obtained from commercial vendors. Additively manufactured samples were prepared using an EOS M290 machine and a laser beam powder bed fusion (LB-PBF) additive manufacturing process, with the manufacturer's recommended process parameters of 280 W laser power, 0.14 mm hatching space, 1200 mm/s scanning speed, and 30 $\mu$m layer thickness using Ti−6Al−4V Powder: LPW-Ti64GD23-AAFD.

**$TiO_2$ Formation Process.** First, the titanium samples were cleaned by acetone and methanol and placed into a custom-built environmental chamber for laser processing. The laser


https://dx.doi.org/10.1021/acsomega.0c01671
ACS Omega 2020, 5, 16744−16751

transformation experiments were performed in an oxygen environment with different flow rates (6−60 SLM) and at room temperature. The chamber was first flushed with oxygen gas for 2 min to ensure the removal of possible air contaminants. Samples were then controllably laser-processed by a 130 W tunable nanosecond fiber laser (1064 nm wavelength, an S-type beam with beam quality ($M^2$) of 1.3, and a beam diameter of 9.5 mm prior to focusing) with a pulse width ranging from 5 to 2000 ns, pulse energy ranging from 0.04 to 1.57 mJ, and a repetition rate ranging from 1 Hz to 4160 kHz. The laser beam was coupled into a galvo scanner with an F-theta lens with a 103 mm focal length producing an 18 $\mu$m focal size and a scan speed ranging from 1 to 5000 mm/s. A laser marking software (Laser Studio Professional) was used to design various patterns and control the process parameters (e.g., power, pulse width, number of pulses, scan speed, repetition rate, and overlap) for each specific pattern.

**Raman Spectroscopy.** A custom-made Raman spectroscopy system was used for optical diagnostics of our laser synthesized $TiO_2$ samples. The measurements were performed in a confocal micro configuration using a 10× microscope objective lens (NA = 0.25). We used a Horiba HR spectrometer with 1200 grooves/mm grating and a laser excitation wavelength of 532 nm for Raman acquisition.

**XRD Measurements.** Thin-film X-ray diffraction (XRD) (Scintag XDS 2000, Franklin, MA) was used to further verify the formation of crystalline $TiO_2$ in these experiments. Samples were rotated 1° away from the copper X-ray source (1.54 Å Cu K$\alpha$) to enhance the X-ray interaction volume with the surface layer. Scans were conducted between 2$\theta$ angles ranging from 24 to 30° at a continuous scan rate of 2°/min. Anatase and rutile have their highest intensity diffraction peaks within this range at 25.3 and 27.5°, respectively. Jade software (Jade 9 MDI, Livermore, CA) was used to identify diffraction peaks.

**Morphology and Structure Analysis.** A scanning electron microscope (SEM: Zeiss Supra 40, Jena, Germany) with an accelerating voltage of 3 kV was used to examine the surface morphology of the laser synthesized oxides at different magnifications. Laser confocal microscopy (Leica TCS SP2, Wetzler, Germany) was used to measure surface roughness of the oxides. The total scan area for each specimen was 1500 $\mu$m × 1500 $\mu$m, and a 1 $\mu$m $z$-axis step size was used. Fiji software was used to process raw image data and build 3D surface profiles of the oxide surfaces.[53]

## ■ ASSOCIATED CONTENT

### Supporting Information

The Supporting Information is available free of charge at https://pubs.acs.org/doi/10.1021/acsomega.0c01671.

Results for additively manufactured TAV samples, high-purity wrought Ti samples, wrought CP Ti Grade 4 samples, cross-section SEM images of wrought TAV, $TiO_2$ quality comparison of laser-generated $TiO_2$ versus commercial powers, and roughness values before laser processing (PDF)

## ■ AUTHOR INFORMATION


### Corresponding Author

**Masoud Mahjouri-Samani** − *Department of Electrical and Computer Engineering and National Center for Additive Manufacturing Excellence (NCAME), Auburn University, Auburn, Alabama 36849, United States;* orcid.org/0000-0002-6080-7450; Email: mahjouri@auburn.edu

### Authors

**Parvin Fathi-Hafshejani** − *Department of Electrical and Computer Engineering, Auburn University, Auburn, Alabama 36849, United States*

**Haden Johnson** − *The Department of Biomedical Materials Science, University of Mississippi Medical Center, Jackson, Mississippi 39216, United States*

**Zabihollah Ahmadi** − *Department of Electrical and Computer Engineering, Auburn University, Auburn, Alabama 36849, United States*

**Michael Roach** − *The Department of Biomedical Materials Science, University of Mississippi Medical Center, Jackson, Mississippi 39216, United States*

**Nima Shamsaei** − *Department of Mechanical Engineering and National Center for Additive Manufacturing Excellence (NCAME), Auburn University, Auburn, Alabama 36849, United States*

Complete contact information is available at: https://pubs.acs.org/10.1021/acsomega.0c01671


### Author Contributions

P.F.-H. designed and performed laser synthesis and processing experiments, materials characterization, and data analysis. Z.A. participated in the laser processing experiment. M.R. and H.J. participated in XRD and SEM characterization, data analysis, and paper preparation. N.S. participated in the experimental design, additive manufacturing sample preparation, and discussions on experimental results. M.M.-S. led the project, participated in experimental design, data acquisition and analysis, discussions, and paper preparation. All of the authors commented on the paper.

### Notes

The authors declare no competing financial interest.

## ■ ACKNOWLEDGMENTS

This material is based upon work partially supported by the U.S. National Science Foundation (NSF) under grant no. 1923363 and the Auburn University Intermural Grant Program (IGP-VPR 180247). The authors would like to thank Fort Wayne Metals (Fort Wayne, IN) for the donations of the wrought TAV and CP Ti Grade 4 materials for the study.

## ■ REFERENCES


(1) Adell, R.; Eriksson, B.; Lekholm, U.; Brånemark, P.-I.; Jemt, T. A long-term follow-up study of osseointegrated implants in the treatment of totally edentulous jaws. *Int. J. Oral Maxillofac. Implants* **1990**, *5*, 347−359.

(2) Geetha, M.; Singh, A.; Asokamani, R.; Gogia, A. Ti based biomaterials, the ultimate choice for orthopaedic implants−a review. *Prog. Mater. Sci.* **2009**, *54*, 397−425.

(3) Carrion, P. E.; Shamsaei, N.; Daniewicz, S. R.; Moser, R. D. Fatigue behavior of Ti-6Al-4V ELI including mean stress effects. *Int. J. Fatigue* **2017**, *99*, 87−100.

(4) Sidambe, A. T. Biocompatibility of advanced manufactured titanium implants—A review. *Materials* **2014**, *7*, 8168−8188.

(5) Liu, X.; Chu, P. K.; Ding, C. Surface modification of titanium, titanium alloys, and related materials for biomedical applications. *Mater. Sci. Eng., R* **2004**, *47*, 49−121.

(6) Kulangara, K.; Leong, K. W. Substrate topography shapes cell function. *Soft Matter* **2009**, *5*, 4072−4076.

(7) Williams, D. F. On the nature of biomaterials. *Biomaterials* **2009**, *30*, 5897−5909.
(8) Higuchi, A.; Ling, Q.-D.; Chang, Y.; Hsu, S.-T.; Umezawa, A. Physical cues of biomaterials guide stem cell differentiation fate. *Chem. Rev.* **2013**, *113*, 3297−3328.
(9) Fattakhova-Rohlfing, D.; Zaleska, A.; Bein, T. Three-dimensional titanium dioxide nanomaterials. *Chem. Rev.* **2014**, *114*, 9487−9558.
(10) Cho, I. S.; Chen, Z.; Forman, A. J.; Kim, D. R.; Rao, P. M.; Jaramillo, T. F.; Zheng, X. Branched $TiO_2$ nanorods for photoelectrochemical hydrogen production. *Nano Lett.* **2011**, *11*, 4978−4984.
(11) Crane, G. M.; Ishaug, S. L.; Mikos, A. G. *Bone Tissue Engineering*; Nature Publishing Group, 1995.
(12) Jokinen, M.; Pätsi, M.; Rahiala, H.; Peltola, T.; Ritala, M.; Rosenholm, J. Influence of sol and surface properties on in vitro bioactivity of sol-gel-derived $TiO_2$ and $TiO_2$-$SiO_2$ films deposited by dip-coating method. *J. Biomed. Mater. Res.* **1998**, *42*, 295−302.
(13) Nygren, H.; Eriksson, C.; Lausmaa, J. Adhesion and activation of platelets and polymorphonuclear granulocyte cells at $TiO_2$ surfaces. *J. Lab. Clin. Med.* **1997**, *129*, 35−46.
(14) Nakata, K.; Fujishima, A. $TiO_2$ photocatalysis: Design and applications. *J. Photochem. Photobiol., C* **2012**, *13*, 169−189.
(15) Bao, S.-J.; Lei, C.; Xu, M.-W.; Cai, C.-J.; Jia, D.-Z. Environment-friendly biomimetic synthesis of $TiO_2$ nanomaterials for photocatalytic application. *Nanotechnology* **2012**, *23*, No. 205601.
(16) Biswas, S.; Becker, U. Molecular modeling of cell adhesion peptides on hydroxyapatite and $TiO_2$ surfaces: implication in biomedical implant devices. *J. Biomater. Nanobiotechnol.* **2013**, *4*, 351.
(17) Ahn, T.-K.; Lee, D. H.; Kim, T.-S.; Jang, G. C.; Choi, S.; Oh, J. B.; Ye, G.; Lee, S. Modification of Titanium Implant and Titanium Dioxide for Bone Tissue Engineering. In *Novel Biomaterials for Regenerative Medicine*; Springer, 2018; pp 355−368.
(18) Wu, S.; Weng, Z.; Liu, X.; Yeung, K.; Chu, P. K. Functionalized $TiO_2$ based nanomaterials for biomedical applications. *Adv. Funct. Mater.* **2014**, *24*, 5464−5481.
(19) Löbl, P.; Huppertz, M.; Mergel, D. Nucleation and growth in $TiO_2$ films prepared by sputtering and evaporation. *Thin Solid Films* **1994**, *251*, 72−79.
(20) Zhao, T.; Zhao, Y.; Jiang, L. Nano-/microstructure improved photocatalytic activities of semiconductors. *Philos. Trans. R. Soc., A* **2013**, *371*, No. 20120303.
(21) Asahi, R.; Morikawa, T.; Irie, H.; Ohwaki, T. Nitrogen-doped titanium dioxide as visible-light-sensitive photocatalyst: designs, developments, and prospects. *Chem. Rev.* **2014**, *114*, 9824−9852.
(22) Pearson, A.; Zheng, H.; Kalantar-Zadeh, K.; Bhargava, S. K.; Bansal, V. Decoration of $TiO_2$ nanotubes with metal nanoparticles using polyoxometalate as a UV-switchable reducing agent for enhanced visible and solar light photocatalysis. *Langmuir* **2012**, *28*, 14470−14475.
(23) Park, E.-J.; Song, Y.-H.; Hwang, M.-J.; Song, H.-J.; Park, Y.-J. Surface characterization and osteoconductivity evaluation of micro/nano surface formed on titanium using anodic oxidation combined with $H_2O_2$ etching and hydrothermal treatment. *J. Nanosci. Nanotechnol.* **2015**, *15*, 6133−6136.
(24) Kokubo, T.; Yamaguchi, S. Bioactive Titanate Layers Formed on Titanium and Its Alloys by Simple Chemical and Heat Treatments. *Open Biomed. Eng. J.* **2015**, *9*, 29.
(25) Roest, R.; Latella, B.; Heness, G.; Ben-Nissan, B. Adhesion of sol−gel derived hydroxyapatite nanocoatings on anodised pure titanium and titanium (Ti6Al4V) alloy substrates. *Surf. Coat. Technol.* **2011**, *205*, 3520−3529.
(26) Huang, H.; Lan, P.-H.; Zhang, Y.-Q.; Li, X.-K.; Zhang, X.; Yuan, C.-F.; Zheng, X.-B.; Guo, Z. Surface characterization and in vivo performance of plasma-sprayed hydroxyapatite-coated porous Ti6Al4V implants generated by electron beam melting. *Surf. Coat. Technol.* **2015**, *283*, 80−88.
(27) Jin, G.; Qin, H.; Cao, H.; Qian, S.; Zhao, Y.; Peng, X.; Zhang, X.; Liu, X.; Chu, P. K. Synergistic effects of dual Zn/Ag ion implantation in osteogenic activity and antibacterial ability of titanium. *Biomaterials* **2014**, *35*, 7699−7713.
(28) Tan, A.; Ismail, R.; Chua, K.; Ahmad, R.; Akbar, S.; Pingguan-Murphy, B. Osteogenic potential of in situ $TiO_2$ nanowire surfaces formed by thermal oxidation of titanium alloy substrate. *Appl. Surf. Sci.* **2014**, *320*, 161−170.
(29) Mahjouri-Samani, M.; Tian, M.; Puretzky, A. A.; Chi, M.; Wang, K.; Duscher, G.; Rouleau, C. M.; Eres, G.; Yoon, M.; Lasseter, J.; et al. Nonequilibrium synthesis of $TiO_2$ nanoparticle "building blocks" for crystal growth by sequential attachment in pulsed laser deposition. *Nano Lett.* **2017**, *17*, 4624−4633.
(30) Tian, M.; Mahjouri-Samani, M.; Eres, G.; Sachan, R.; Yoon, M.; Chisholm, M. F.; Wang, K.; Puretzky, A. A.; Rouleau, C. M.; Geohegan, D. B.; Duscher, G. Structure and formation mechanism of black $TiO_2$ nanoparticles. *ACS Nano* **2015**, *9*, 10482−10488.
(31) Dumitriu, D.; Bally, A.; Ballif, C.; Hones, P.; Schmid, P.; Sanjines, R.; Levy, F.; Parvulescu, V. Photocatalytic degradation of phenol by $TiO_2$ thin films prepared by sputtering. *Appl. Catal., B* **2000**, *25*, 83−92.
(32) Takeda, S.; Suzuki, S.; Odaka, H.; Hosono, H. Photocatalytic $TiO_2$ thin film deposited onto glass by DC magnetron sputtering. *Thin Solid Films* **2001**, *392*, 338−344.
(33) Zhang, F.; Huang, N.; Yang, P.; Zeng, X.; Mao, Y.; Zheng, Z.; Zhou, Z.; Liu, X. Blood compatibility of titanium oxide prepared by ion-beam-enhanced deposition. *Surf. Coat. Technol.* **1996**, *84*, 476−479.
(34) Gaviria, L.; Salcido, J. P.; Guda, T.; Ong, J. L. Current trends in dental implants. *J. Korean Assoc. Oral Maxillofac. Surg.* **2014**, *40*, 50−60.
(35) Lifland, M.; Kim, D.; Okazaki, K. Mechanical properties of a Ti-6A1-4V dental implant produced by electro-discharge compaction. *Clin. Mater.* **1993**, *14*, 13−19.
(36) Wang, X.; Li, Y.; Hodgson, P. D.; Wen, C. Biomimetic modification of porous TiNbZr alloy scaffold for bone tissue engineering. *Tissue Eng., Part A* **2010**, *16*, 309−316.
(37) Yang, B.; Mahjouri-Samani, M.; Rouleau, C. M.; Geohegan, D. B.; Xiao, K. Low temperature synthesis of hierarchical $TiO_2$ nanostructures for high performance perovskite solar cells by pulsed laser deposition. *Phys. Chem. Chem. Phys.* **2016**, *18*, 27067−27072.
(38) Benea, L.; Mardare-Danaila, E.; Celis, J.-P. Increasing the tribological performances of Ti−6Al−4V alloy by forming a thin nanoporous $TiO_2$ layer and hydroxyapatite electrodeposition under lubricated conditions. *Tribol. Int.* **2014**, *78*, 168−175.
(39) Cheng, Y.; Yang, H.; Yang, Y.; Huang, J.; Wu, K.; Chen, Z.; Wang, X.; Lin, C.; Lai, Y. Progress in $TiO_2$ nanotube coatings for biomedical applications: a review. *J. Mater. Chem. B* **2018**, *6*, 1862−1886.
(40) Jain, S.; Williamson, R. S.; Roach, M. D. Surface characterization, shear strength, and bioactivity of anodized titanium prepared in mixed-acid electrolytes. *Surf. Coat. Technol.* **2017**, *325*, 594−603.
(41) Roach, M. D.; Williamson, R. S.; Blakely, I. P.; Didier, L. M. Tuning anatase and rutile phase ratios and nanoscale surface features by anodization processing onto titanium substrate surfaces. *Mater. Sci. Eng., C* **2016**, *58*, 213−223.
(42) Joo, H.-C.; Lim, Y.-J.; Kim, M.-J.; Kwon, H.-B.; Han, J.-H. Characterization on titanium surfaces and its effect on photocatalytic bactericidal activity. *Appl. Surf. Sci.* **2010**, *257*, 741−746.
(43) Sumita, T.; Yamaki, T.; Yamamoto, S.; Miyashita, A. Photo-induced surface charge separation of highly oriented $TiO_2$ anatase and rutile thin films. *Appl. Surf. Sci.* **2002**, *200*, 21−26.
(44) Luttrell, T.; Halpegamage, S.; Tao, J.; Kramer, A.; Sutter, E.; Batzill, M. Why is anatase a better photocatalyst than rutile?—Model studies on epitaxial $TiO_2$ films. *Sci. Rep.* **2014**, *4*, No. 4043.
(45) Bickley, R. I.; Gonzalez-Carreno, T.; Lees, J. S.; Palmisano, L.; Tilley, R. J. D. A structural investigation of titanium dioxide photocatalysts. *J. Solid State Chem.* **1991**, *92*, 178−190.
(46) Su, R.; Bechstein, R.; Sø, L.; Vang, R. T.; Sillassen, M.; Esbjörnsson, B.; Palmqvist, A.; Besenbacher, F. How the Anatase-to-


https://dx.doi.org/10.1021/acsomega.0c01671
*ACS Omega* 2020, 5, 16744−16751

Rutile Ratio Influences the Photoreactivity of $TiO_2$. *J. Phys. Chem. C* **2011**, *115*, 24287−24292.
(47) Hurum, D. C.; Agrios, A. G.; Gray, K. A.; Rajh, T.; Thurnauer, M. C. Explaining the Enhanced Photocatalytic Activity of Degussa P25 Mixed-Phase $TiO_2$ Using EPR. *J. Phys. Chem. B* **2003**, *107*, 4545−4549.
(48) Xiong, W.; Zhou, Y.; Hou, W.; Jiang, L.; Mahjouri-Samani, M.; Park, J.; He, X.; Gao, Y.; Fan, L.; Baldacchini, T.; et al. Laser-based micro/nanofabrication in one, two and three dimensions. *Front. Optoelectron.* **2015**, *8*, 351−378.
(49) Wang, X.; Xu, X. Thermoelastic wave induced by pulsed laser heating. *Appl. Phys. A* **2001**, *73*, 107−114.
(50) Xiong, W.; Zhou, Y.; He, X.; Gao, Y.; Mahjouri-Samani, M.; Baldacchini, T.; Lu, Y. In *Three-Dimensional Micro/Nano-Fabrication by Integration of Additive and Subtractive Femtosecond-Laser Direct Writing Processes*, International Congress on Applications of Lasers & Electro-Optics; LIA, 2012; pp 1160−1164.
(51) Su, W.; Zhang, J.; Feng, Z.; Chen, T.; Ying, P.; Li, C. Surface phases of $TiO_2$ nanoparticles studied by UV Raman spectroscopy and FT-IR spectroscopy. *J. Phys. Chem. C* **2008**, *112*, 7710−7716.
(52) Spurr, R. A.; Myers, H. Quantitative Analysis of Anatase-Rutile Mixtures with an X-Ray Diffractometer. *Anal. Chem.* **1957**, *29*, 760−762.
(53) Schindelin, J.; Arganda-Carreras, I.; Frise, E.; Kaynig, V.; Longair, M.; Pietzsch, T.; Preibisch, S.; Rueden, C.; Saalfeld, S.; Schmid, B.; Tinevez, J.-Y.; White, D. J.; Hartenstein, V.; Eliceiri, K.; Tomancak, P.; Cardona, A. Fiji: an open-source platform for biological-image analysis. *Nat. Methods* **2012**, *9*, 676−682.



https://dx.doi.org/10.1021/acsomega.0c01671
*ACS Omega* 2020, 5, 16744−16751